Aerodynamic features of a two-airfoil arrangement

Thierry M. Faure · Laurent Hétru · Olivier Montagnier

Abstract The interaction between two foils occurs in many aerodynamic or hydrodynamic applications. Although the characteristics of many airfoils are well-documented, there is a limited amount of data for multiple airfoils in interaction and for large values of the angle of attack. This paper presents measurements of the turbulent flow around a two-airfoil T-tail type arrangement and the aerodynamic coefficients, for an incompressible flow at moderate Reynolds number. The study focuses mainly on large angles of attack, corresponding to detached flows on the airfoils, large wakes and involving vortex shedding. Phase averages of velocity fields are made building the flow time development relative to the vortex shedding. The understanding of the change in the tail lift coefficient versus angle of attack, between a two-airfoil arrangement and a single airfoil, is discussed in relation with the position and width of the wing wake and the pathlines of the shedding vortices.

1 Introduction

Aerodynamics of airfoils in incompressible flow, operated on moderate Reynolds numbers in the range 10^4

Thierry M. Faure · Laurent Hétru · Olivier Montagnier
Centre de Recherche de l'Armée de l'air, École de l'Air, F-13661 Salon-de-Provence, France
e-mail: thierry.faure@defense.gouv.fr

Olivier Montagnier
Laboratoire de Mécanique et d'Acoustique, Aix-Marseille Université, Centre National de la Recherche Scientifique, Unité Propre de Recherche 7051, Centrale Marseille, F-13453 Marseille cedex 13, France

to 10^5, has recently gained in importance, with a variety of applications, such as unmanned air vehicles (UAV), micro air vehicles (MAV), high altitude long endurance aircrafts (HALE) (Mueller and DeLaurier (2003)) and propulsive hydrodynamic systems (Anderson et al (1998)). Many studies are focusing on rotor aircraft but there is a lack of publication on classical wing-tail arrangement for that Reynolds number range. A possible application is the understanding of one of the many issues present in the deep stall phenomenon, typical of large angles of attack for T-tail aircraft configurations, where the tail is flying in the detached flow of the wing (Taylor and Ray (1965)). That attitude corresponds to a stable equilibrium point, where the pitch command is highly ineffective, making simple stall recovery procedures inappropriate.

Many studies have been conducted on the detached flow around an airfoil, marked by a suction side recirculation, the development of an instability from the leading edge detachment point, and the adaptation of the leading edge circulation for the enforcement of the Kelvin theorem. These latter effects induce periodic vortex shedding resulting in the development of downstream vortex streets. If most of the airfoils are well-documented for values of the angle of attack lower than the stall angle, few references report results for detached flows. The diagram of the types of shedding development with Reynolds number and angle of attack is published for a NACA 0012 in Huang and Lee (2000), Huang and Lin (1995) and Wu et al (1998). Devinant et al (2002) measured the forces and the pitching moment on a NACA 65_4-421 airfoil for values of the angle of attack between $-10°$ and $90°$ and for Reynolds numbers between 2×10^5 and 7×10^5. The aim of this work is to relate the upstream turbulence level with aerodynamic characteristics. For a very low turbulence level of

0.5%, these authors find the independance of the aerodynamic coefficients with Reynolds number for $\alpha \geq 23°$. Measurements of Alam et al (2010) are conducted with a NACA 0012 for angles of attack $-10° \leq \alpha \leq 90°$ and Reynolds numbers in the range 5.3×10^3 to 5.1×10^4. The Strouhal number, matching with the vortex shedding instability, decreases with the increasing angle of attack, and reaches a threshold for $\alpha \geq 60°$. Lee and Su (2012) compared the lift and drag coefficients for a NACA 0012 and a flat plate, for Reynolds numbers between 2×10^4 and 7.5×10^4. They obtained the aerodynamics loads by integration of the velocity obtained with particle image velocimetry.

As previously mentioned, most of the available studies on airfoils concern attached or near-stall flows. The original study of Bourgoyne et al (2005) explores the flow around a hydrofoil with a suction side corresponding to a NACA 16 and a flat pressure side after 28% of the chord, for an angle of attack of zero and a range of Reynolds numbers $1.4 \times 10^6 \leq Re \leq 5 \times 10^7$. Measurements focus on the flow near the trailing edge and on the effect of a geometry modification of that part in the flow morphology. The trailing edge vortex shedding from the boundary layers are observed by space phase averages and spectral analysis. However, most of the experimental flow characterisation around airfoils are conducted for much lower Reynolds numbers. Yarusevych et al (2009) study the vortex shedding frequency downstream of a NACA 0025 airfoil for $\alpha = 0°, 5°, 10°$ and Reynolds numbers in the range $5.5 \times 10^4 \leq Re \leq 2.1 \times 10^5$. These authors are mainly interested in the boundary layer transition. Laitone (1997) compares forces coefficients for $Re \leq 7 \times 10^4$ on a NACA 0012 airfoil, a flat plate and a cambered plate. A slender leading edge induces a better lift for $Re \leq 2 \times 10^4$, and the NACA 0012 is not adapted for $Re \leq 5 \times 10^4$ because of its sensitivity to Reynolds number or upstream turbulence level. Ravi et al (2012) consider a thin airfoil with an elliptical leading edge for low Reynolds numbers between 3×10^4 and 1.1×10^5 . The study focuses on the vortex shedding frequency of the leading edge vortices and the dependance on upstream turbulence level.

The vortex shedding for a two-cylinder arrangement have been extensively studied (Sumner et al (2000), Alam and Sakamoto (2005), Sumner et al (2008), Hu and Zhou (2008a) and Hu and Zhou (2008b)) with recent reviews on this topic (Sumner (2010) and Zhou and Alam (2016)). The flow detachment position on a cylinder changes with Reynolds number and is different from an airfoil, where shear layers are originating from the leading and trailing edges. However, for completely detached configurations, and regimes with an established Kármán votex street, some features are comparable.

Few publications concerning aerodynamic interaction between two airfoils are available. Lee (2011) consider the flow around tandem NACA 0012 airfoils oscillating in phase or opposite in phase, but the static case is also considered. Pressure distribution and velocity field are obtained experimentally. An hysteresis is present in the dynamical development of the aerodynamic coefficients. The flow downwash caused by the upstream airfoil, modifies the generation of the leading edge vortex on the downstream airfoil. This is reflected by the reducing effect of the generation of the leading edge vortex and an hysteresis much smaller in comparison with the case with no upstream airfoil. In addition, the distance between the airfoils and the phase-shift drive the interaction intensity. Scharpf and Mueller (1992) study the aerodynamic forces developed by Wortmann $FX63-137$ airfoils in tandem for a Reynolds number of 8.5×10^4. The various geometrical settings between the airfoils evidence an increase in the lift-drag ratio of the downstream airfoil reaching 77% comparing single and tandem arrangements. However, the study is limited to angles of attack $-15° \leq \alpha \leq 20°$. Jones et al (2015) are interested in the aerodynamics around a two-flat plate arrangement for a Reynolds number $Re = 10^5$, and conduct a parametrical analysis of the distance between the plates. The gap between them, measured from the half-chord, varies from 0 to $1.5c$ in the upstream flow direction and the stagger from $-1.5c$ and $1.5c$ in the direction perpendicular to the upstream flow. PIV measurements prove that the increase of the aerodynamic efficiency of the downstream airfoil is strongly dependant on the flow strength between the airfoils and on the interaction between the shear layer of the upstream airfoil with the downstream airfoil. Khan and Mueller (1991) studied a canard/wing arrangement focusing on three-dimensional effects produced by the canard tip vortex interaction with the wing, for a Reynolds number of 1.5×10^5.

The interaction between an airfoil and a vortex advected in a flow is also a topic related to the aerodynamic interaction, when vortex shedding occurs from the upstream airfoil detached flow. Świrydczuk (1990) conducts flow visualisations from a vortex and a symetrical airfoil with a maximum thickness/chord ratio of 5% at a Reynolds number of 4.5×10^3. The vortex shedding at a distance of 0.4 chord above the airfoil induces a trailing edge counter-rotating vortex, from the conservation of circulation imposed by the Kelvin theorem. That vortex generation is connected with a decrease on the strength of the upstream vortex. Horner et al (1993) analysed the time modulation of the aerodynamic coefficients resulting from the interaction between a vortex and a NACA 0015 airfoil. Favier et al (1987) study the

interaction between a wing tip vortex generated by an upstream airfoil on an oscillating downstream airfoil. A two-dimensional analysis of the influence of a vortex advected by the flow on a NACA 0012 airfoil was analysed with a potential method by Coronado Domenge and Ilie (2012).

In order to get the aerodynamic coupling between the vortices generated by the detached flow from an upstream airfoil (wing) on a downstream airfoil (tail of half the wing chord), a two-dimensional benchmark experiment is developed in the present study for velocity and force characterisation. The aim is to understand the flow properties resulting from the wakes interaction and the influence of the detached flow region with the angle of attack, but also to catch the dynamics of vortices, created by the development of vortex shedding. Velocity measurements are conducted with particle image velocimetry (PIV) and the aerodynamic coefficients on each airfoil are obtained by strain gauges balances. The mean velocity field and its turbulence characteristics are analysed comparing the single airfoil and the two-airfoil arrangement in order to evidence the influence of the wing on the tail. The aerodynamic coefficients are also presented for both airfoil configuration. The wing vortex shedding mechanism, observed for detached flow configurations at high values of the angle of attack, is expanded with vortex circulation measurements in order to conclude on the origin of the interaction between the airfoils observed in the aerodynamic coefficients.

2 Experimental set-up and apparatus

2.1 Facility

The experiment is achieved with a closed-loop wind tunnel capable of steady flows from 5 to $45\,\mathrm{m.s^{-1}}$, with a squared test section $450\,\mathrm{mm} \times 450\,\mathrm{mm}$ and $650\,\mathrm{mm}$ in length. The velocity inside the test section is homogeneous with deviations lower than 1% and a residual turbulence lower than 0.3%. The x-axis is the upstream flow direction, the y-axis is the airfoils span direction and the z-axis is orthogonal to x and y. The experimental setup is made of two NACA 23 012 airfoils placed in the test section (figure 1), the chord $c_W = c$ of the upstream airfoil, referred as the wing, is twice the chord of the downstream airfoil $c_T = c/2$, referred as the tail, both of them get a span equal to the width of the test section. The distance between the airfoils can be changed along two perpendicular directions (figure 2). Hereafter, the distances between the leading edges of the two airfoils, in the upstream airfoil (wing) frame of reference, are $L = 3c$ and $H = c$. That arrangement is

typical of a T-tail airplane configuration. The Reynolds number Re is based on the chord and the usptream velocity U_∞. Each airfoil is supported on a single axis, placed at the quarter-chord, and fixed to a rotating disk in one wall of the wind tunnel, allowing the angle of attack setting and providing a free optical access from the other side of the wind tunnel. The actual angle, corresponding to an airfoil angle of attack of 0°, is measured with an uncertainty of ±0.2°, fitting the measured lift coefficient with the actual value obtained from literature (Abbott and Von Doenhoff (1949)). After that setting, the accuracy corresponding to a change in the angle of attack is obtained with an optical encoder with an uncertainty of ±0.01°. In addition, the tail airfoil can be adjusted from the wing with a setting angle i_T with an uncertainty of ±0.2° (figure 2). The angle setting is performed in the same way as for the wing. Hereafter, i_T is set to 0° for each configuration. The main drawbacks of this setup are high aspect ratios for both airfoils, 9 for the wing and 18 for the tail. As the wing and tail are clamped in only one side of the wind tunnel, they are subject to structural bending modes. In order to avoid flow disturbances by these bending frequencies, it is necessary to shift them to higher values. To do this, the wings are made of carbon fibres aligned with the span direction. The wings aspect ratios may result in buffeting for high velocities, limiting the upstream flow velocity to $17.5\,\mathrm{m.s^{-1}}$ for the two-airfoil arrangement. The wind tunnel geometric blockage is defined by Hétru (2015) as:

$$B = \frac{S_1 \cup S_2}{S} \tag{1}$$

where S is the wind tunnel area, S_1 and S_2 the wing and tail projected area respectively.

To limit the blockage for high values of angle of attack, a chord $c = 50\,\mathrm{mm}$ is chosen for the wing, leading to an angle of attack of 30° with a blockage ratio lower than 6% (figure 3) below which there is no flow distortion and no necessary correction on the aerodynamic forces (West and Apelt (1982)). The drop of the blockage observed between 22° and 30° corresponds to the positions of the tail masked by the wing. A similar tunnel blockage of 6% (Bourgoyne et al (2003)) or slightly exceeding that value up to 9% (Sicot et al (2006)) can be found in other studies. There is also a wake blockage due to the wake width growing downstream of each airfoil. However, as far as the study is limited to near-wake flow dynamics and that the wake width is rather limited in that region, there is no noticeable influence of that growth on the blockage. The upstream airfoil (wing) is placed in the centre of the test section, and its axis is parallel to the axis of the rotation setting. In addition, because of the angle of attack limitation to
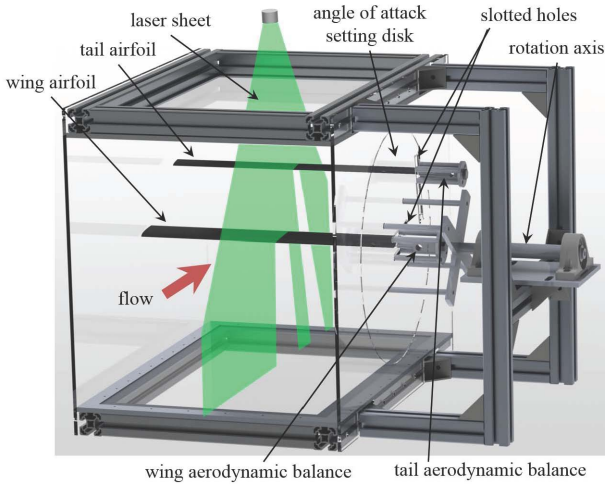
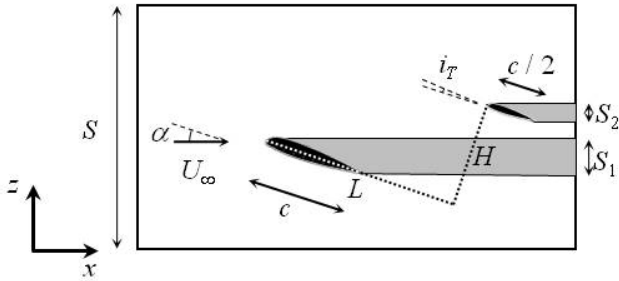Fig. 1: Test section and experimental set-up.

Fig. 2: Two-airfoil arrangement and flow geometric blockage.

Fig. 3: Blockage of the two-airfoil arrangement versus angle of attack (the airfoil thickness is neglected).

30°, the tail is always above $3c$ from the wind tunnel floor, avoiding any ground effect interference, which influence is sensitive up to one chord (Katz and Plotkin (2001)).

The Reynolds number based on the wing chord is equal to 5.83×10^4 and to 2.92×10^4 for the tail, with additional measurements at 1.16×10^5 obtained for the wing with an upstream flow velocity of $35\,\text{m.s}^{-1}$. The similarity between the experiment and unmanned air vehicle (UAV), micro air vehicle (MAV) or high altitude long endurance aircraft (HALE) applications is generally respected, but not between the experiment and traditional aircrafts in cruise flight conditions.

2.2 Instrumentation

Lift, drag and pitching moment coefficients are measured for each airfoil with strain gauge balances. These balances, developed for this study, consist in specific pieces placed between each airfoil and the rotation disk allowin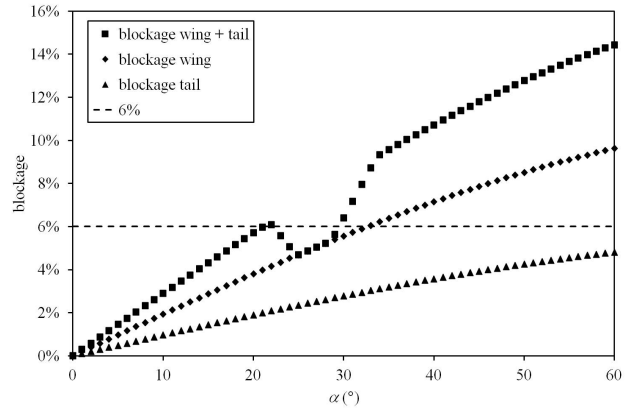g the angle of attack setting. These pieces are aluminium rectangular blocks with two perpendicular holes allowing the strain concentration on peculiar regions of the device. The size of the strain gauge films is $14\,\text{mm} \times 7\,\text{mm}$ and these gauges are sticked on the piece opposite to each hole. A bending measurement is obtained with two gauge films placed symmetricaly on the piece. The forces are recorded by an analog/digital converter National Instrument DAQ-NI 9219 with a sampling frequency of $100\,\text{Hz}$ and recorded on National Instrument LabView. The weight offset of each airfoil is cancelled by an appropriate procedure before each measurement (Hétru (2015)). The uncertainty on the measured forces is estimated to $0.1\,\text{N}$. In addition to strain gauge balances, the incremental encoder used for the measurement of the angle of attack is also recorded on LabView.

Flow seeding is obtained with a nebuliser providing dropplets of Di-Etyl-Hexyl-Sebacate with an average diameter of $1\,\mu m$ and injected downstream of the test section. PIV frames are recorded by a 12-bit camera with a resolution 2360×1776 pixels and a frequency of 15 Hz. The PIV frames cover an area of 400×300 mm. A Nd:YAG laser is emitting a wavelength 532 nm to generate a light sheet of 0.5 mm in thickness with 200 mJ by pulse. The laser is placed above the test section and the laser sheet is shadowed by the airfoils. Their pressure sides are not lightened, where no velocity field is obtained. However, as the study focuses on flow detachement on the suction side for large values of the angle of attack, the lack of information on that side is not a great concern. PIV frames are filtered from spurious light reflections and low density seeding regions with a linear subtraction filter of a background noise frame. This frame is the average of the frames recorded for a given configuration. Velocity fields are obtained

with LaVision Davies software with an interrogation window of 32×32 pixels and an overlap of 75%. Averaged velocity and standard deviation of fluctuations are obtained from 500 fields to get uncertainties lower than 1%. In order to get a maximum view of the flow, the camera framing is fitted in order to get a complete view of the airfoil suction side.

3 Flow development with angle of attack

Figure 4 shows the normalised averaged streamwise velocity $\bar{U}_x/U_\infty$ for the single-airfoil arrangement (only the wing inside the wind tunnel) and for the 2-airfoil arrangement (wing and tail inside the wind tunnel), for three values of the angle of attack. For $\alpha = 0°$ the flow is attached (figure 4a), and the suction side of the airfoil near the leading edge is marked by a region of high velocity corresponding to a maximum suction. For $\alpha = 15°$ (figure 4c) the suction side flow is completely detached (as will be shown later, the airfoil stall angle is 7° for that Reynolds number), a low velocity region is observed on the airfoil suction side, bounded by two regions of large velocity. The transition between the low and large velocity regions corresponds to the flow shear between the upstream flow accelerated by the airfoil streamlines deviation, and the detached recirculating flow. An instability develops in that strong shear region, but is not observed in averaged velocity fields. For $\alpha = 30°$ (figure 4e) the recirculation region is larger and wider than for $\alpha = 15°$. The same values of the angle of attack are presented for the 2-airfoil arrangement with $L = 3c$ and $H = c$. A small decrease in the high velocity region is observed near the leading edge on the wing for $\alpha = 0°$ (figure 4b), with a similar feature on the tail. For $\alpha = 15°$ (figure 4d) the flow around the wing does not seem to change much from the single-airfoil arrangement. The tail is placed inside the wing wake but sufficiently downstream to develop a little recicultation region on its suction side. For $\alpha = 30°$ (figure 4f), the flow around the wing is still very similar to the single-airfoil arrangement. The tail is placed below the wing wake, but develops a relative larger recirculation region on its detached suction side, because the chord of the tail is half that of the wing. This effect results from the interaction with the wing wake. Note that there is no region of large velocity bounding the tail recirculation region, since the tail is placed close to the wing wake.

Quantitative information is obtained by velocity profiles extracted from the previous PIV fields at axial positions downstream of the wing $x/c = 1.5$ and 2.5 and at 1 and 2 wing chords downstream of the tail, corresponding to $x/c = 4.5$ and 5.5. The comparison between the single-airfoil arrangement (wing) and the 2-airfoil arrangement (wing and tail) is chosen to characterise the effect of interaction. The axial velocity for $\alpha = 0°$ (figure 5a) shows a small velocity defect at $z/c = 0$ associated with the wing wake for both arrangements. The amplitude of the velocity defect is decaying with the axial distance x/c. For the 2-airfoil arrangement, in addition to the wing wake, the velocity defect associated with the wake of the tail is observed at $z/c = 1$, for $x/c = 4.5$ and 5.5. Note that the two wakes present small velocity defects and are spatially decoupled. For $\alpha = 15°$, the flow is completely detached on each airfoil suction side, resulting in lager and deeper wakes (figure 5b). For $x/c = 1.5$ the influence of the flow acceleration regions bounding the detached recirculating flow is evidenced by normalised axial velocities larger than one at $z/c = \pm 0.3$. As the tail is placed behind the wing, both wakes are centred around $z/c = -0.05$. There is no discrepancy, within the measurement uncertainty, between the profiles obtained at $x/c = 1.5$ and 2.5 for the single-airfoil and 2-airfoil arrangements, indicating that there is no noticeable forward potential effect from the tail on the wing wake development. For that value of the angle of attack, the tail is inside the wing wake. The profiles at $x/c = 4.5$ and 5.5 show a wider and deeper velocity defect in comparison with the single-airfoil arrangement. The wake is even wider and deeper for the single-airfoil arrangement and $\alpha = 30°$ (figure 5c), with a centre around $z/c = -0.2$. Similarly, for $x/c = 1.5$ normalised axial velocities larger than one are measured at $z/c = -0.7$ and 0.4, resulting from the flow acceleration around the detached flow. For the 2-airfoil arrangement, there is no influence of the tail on the development of the wing wake for $x/c = 1.5$ and 2.5. For $x/c = 4.5$ and 5.5, the wing and tail wakes are merging into an asymmetric wake centred around $z/c = -0.8$. Note for these profiles that the wake interaction is not a linear summation since the velocity defect of the wing wake at $z/c = -0.2$ is decreased from the single-airfoil arrangement.

The flow turbulent characteristics are analysed with the standard deviation of the axial velocity fluctuations. For $\alpha = 0°$ (figure 6a) the normalised standard deviation of the axial velocity fluctuations σ_x/U_∞ presents a small increase inside the wakes of the wing and tail. These levels are increased by almost a factor of 10 when the flow is detached for $\alpha = 15°$ (figure 6b). Station $x/c = 1.5$ shows a maximum centred on the wake, which evolves for $x/c = 2.5$ into a profile with two successive extrema, typical of the turbulence intensity inside a developed wake. For $x/c = 4.5$ and 5.5, the two extrema are merging into a central maximum. There are little discrepancies between the single-airfoil and the 2-airfoil arrangements since the two airfoils and their wakes are
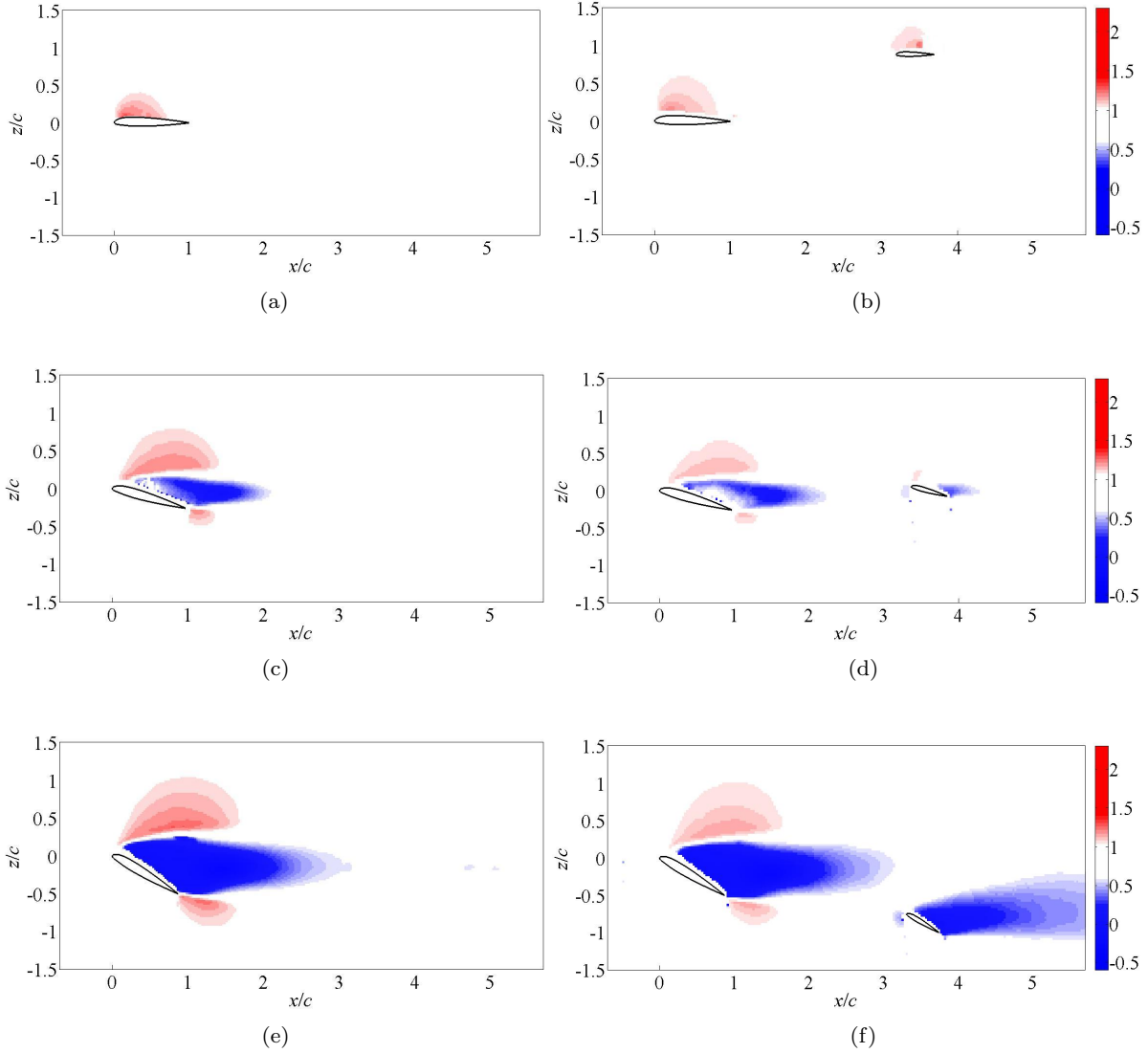
Fig. 4: PIV-measured normalised averaged streamwise velocity $\bar{U}_x/U_\infty$ for the single-airfoil arrangement (left) and the two-airfoil arrangement (right) with $L = 3c$ and $H = c$: (a) single-airfoil $\alpha = 0°$, (b) two-airfoil $\alpha = 0°$, (c) single-airfoil $\alpha = 15°$, (d) two-airfoil $\alpha = 15°$, (e) single-airfoil $\alpha = 30°$, (f) two-airfoil $\alpha = 30°$.

aligned. Similar comments can be made for $\alpha = 30°$ (figure 6c), with two extrema observed at $x/c = 1.5$ resulting from a wider wake. Note, for the 2-airfoil arrangement at $x/c = 4.5$ and $x/c = 5.5$, a larger wake with higher values of σ_x/U_∞ caused by the interaction between the wakes of the wing and the tail which are not aligned for that value of the angle of attack.

The behaviour of the normalised standard deviation of the transverse velocity fluctuations σ_z/U_∞ is similar to σ_x/U_∞ and is not presented.

4 Aerodynamic coefficients

4.1 Lift and drag coefficients development with angle of attack

A complete data base of lift and drag coefficients is obtained for the NACA 23 012 airfoil and angles of attack between $-20°$ and $30°$, including values beyond the airfoil stall. Despite the low wind-tunnel blockage, a correction of the local flow velocity, using flow rate con-
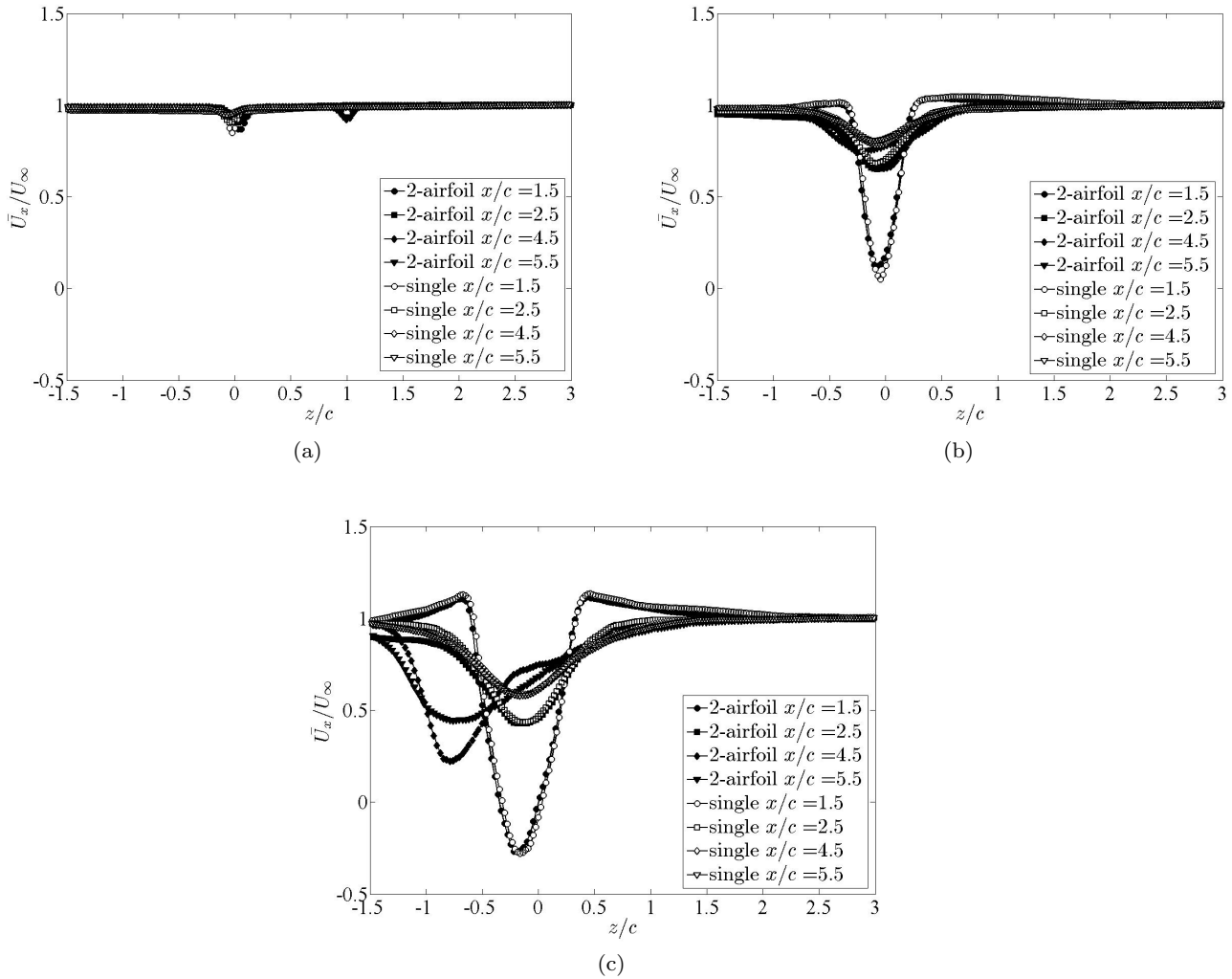
Fig. 5: PIV-measured normalised averaged streamwise velocity $\bar{U}_x/U_\infty$ for the single and two-airfoil arrangements with $L = 3c$ and $H = c$ at varying $x/c = 1.5$, 2.5, 4.5, 5.5 for (a) $\alpha = 0°$, (b) $\alpha = 15°$, (c) $\alpha = 30°$.

servation, is considered in the expressions of the aerodynamic coefficients, which are based on the square of upstream velocity. Such aerodynamic coefficients are not available in literature for this airfoil, but for a symmetrical airfoil of same thickness, the NACA 0012 (Wang et al (2014)), with experimental conditions summarised in table 1. The comparison of the lift coefficient, for the single wing and single tail NACA 23 012 airfoil and these previous data is given in figure 7a. Note a dispersion between the points for the NACA 0012 , due to different Reynolds numbers, wing aspect ratios and wind tunnel upstream turbulence intensities, modifying the stall angle and the maximum lift coefficient. In order to provide a better comparison, the lift coefficients for the NACA 23 012 airfoil for the wing and tail are

plotted versus the angle of attack corrected by the zero lift angle of attack $\alpha - \alpha_{L=0}$ and compared in figure 7b with measurements obtained in closed flow conditions for a NACA 0012 (Laitone (1997)). A very good agreement is found between 0° and 15° for the tail, whose Reynolds number, upstream turbulence level and aspect ratio are very close to the ones of Laitone (1997). The corrected stall angle of attack of the tail is equal to $\alpha - \alpha_{L=0} = 7.5°$ which is in perfect accordance with the measurements of Laitone (1997). Note that the discrepancy of the lift coefficient of Laitone (1997) for $\alpha > 15°$ is probably due to an influence of the aspect ratio (6 versus 18 for the tail in present study).

The lift and drag coefficients are compared for the single-wing or single-tail arrangements (figure 8) and
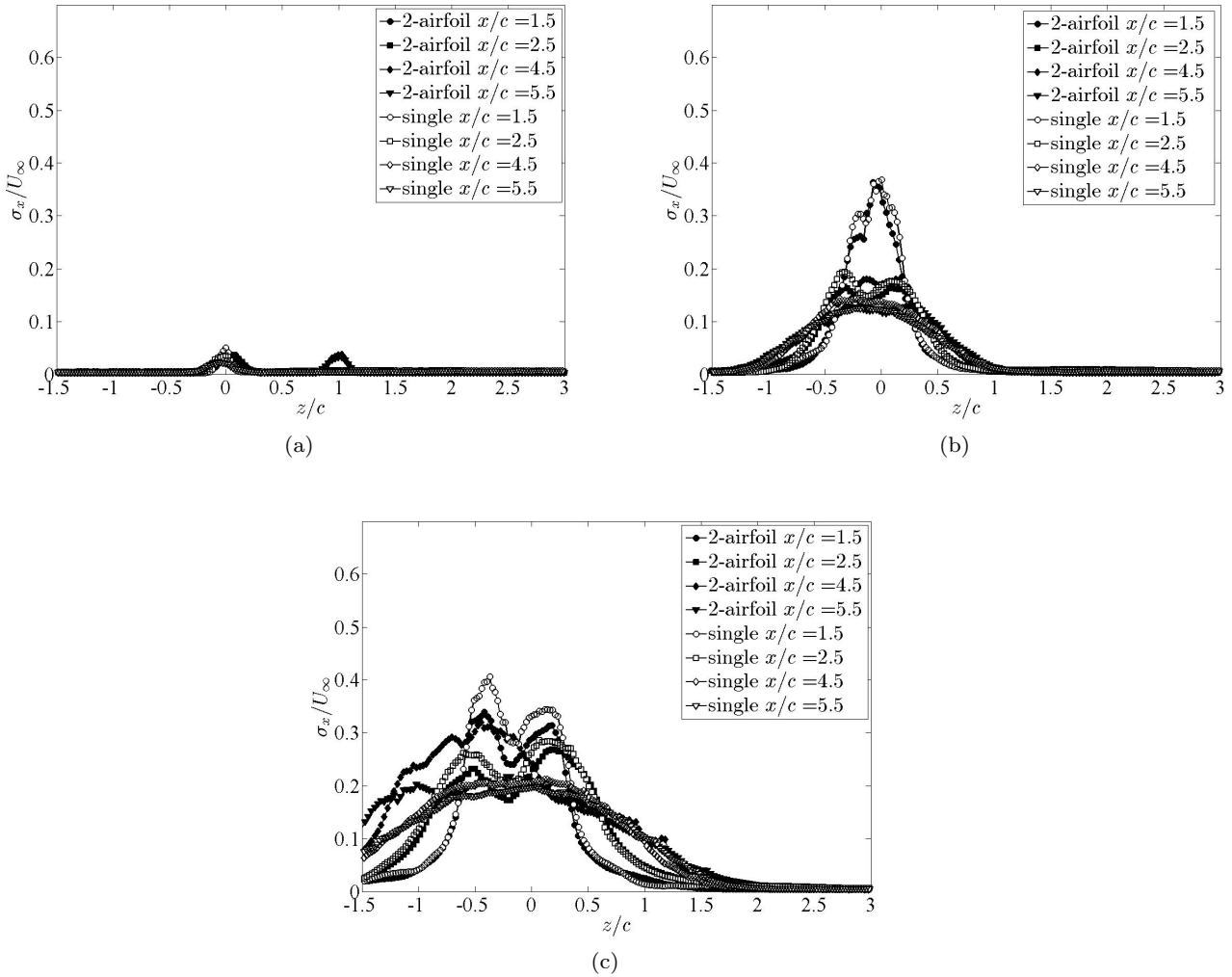
Fig. 6: PIV-measured normalised streamwise velocity standard deviation σ_x/U_∞ for the single and two-airfoil arrangements with $L = 3c$ and $H = c$ at varying $x/c = 1.5$, 2.5, 4.5, 5.5 for (a) $\alpha = 0°$, (b) $\alpha = 15°$, (c) $\alpha = 30°$.

the two-airfoil arrangement (figure 9). For the single-wing or single-tail arrangement, the lift and drag coefficients show the same behaviour for the wing and for the tail, but the stall point is different and corresponds to $\alpha = 7°$ for the wing and $\alpha = 4°$ for the tail (figure 8). As previously mentionned, this difference is due to an effect of the Reynolds number corresponding to 58300 for the wing (chord c) and to 29150 for the tail (chord $c/2$). For the tail, the accordance of the stall angle with the experimental value on the NACA 0012 airfoil for $Re = 2.07 \times 10^4$ is shown in figure 7b. After a decrease following the stall, the lift coefficient increases again from α around 10°. A similar development is found for both airfoils. The data for the single-airfoil arrangement are in agreement with published lift coefficients for a

similar Reynolds number (Alam et al (2010)). Drag coefficients are very similar with very low values in the attached flow region, between $-3°$ and $7°$ for the wing and between $-3°$ and $4°$ for the tail. For the two-airfoil arrangement with $L = 3c$ and $H = c$ (figure 9), lift and drag coefficients for the wing are not changed in comparison with the single-wing arrangement, proving there is no noticeable forward potential effect caused by the tail. For the tail, the lift coefficient is similar to the single-airfoil arrangement for $\alpha < 4°$ corresponding to attached flow conditions. However, for positive values of the angle of attack, no stall drop is observed for the two-airfoil arrangement for $\alpha \geq 4°$. The lift coefficient of the tail shows a continuous rise with a lower slope, in comparision with lower values of the angle of attack.

Researchers	Airfoil	Re	A_R	Tu (%)	Setting	Max.blockage
Critzos et al (1955)	NACA 0012	1.8×10^6	6	not given		5.57×10^{-2}
Lee and Su (2012)	NACA 0012	5.4×10^4	2.53	not given	end plates	8.09×10^{-2}
Lee and Su (2012)	NACA 0012	2.9×10^4	2.53	not given	end plates	6.82×10^{-2}
Laitone (1997)	NACA 0012	2.07×10^4	6	0.1		3.68×10^{-3}
Wang et al (2014)	NACA 0012	2×10^4	2.7	0.6	end plates	6.34×10^{-2}
Cleaver et al (2011)	NACA 0012	2×10^4	3	0.5		4.01×10^{-2}
Cleaver et al (2011)	NACA 0012	10^4	3	0.5		4.01×10^{-2}
Wang et al (2014)	NACA 0012	5.3×10^3	2.7	0.6	end plates	6.34×10^{-2}
Sunada et al (2002)	NACA 0012	4×10^3	7.25	not given		9.92×10^{-3}
present meas. (wing)	NACA 23 012	5.83×10^4	9	0.3		4.69×10^{-2}
present meas. (tail)	NACA 23 012	2.92×10^4	18	0.3		2.35×10^{-2}

Table 1: Selected experimental studies providing the lift coefficient of a 12% thickness airfoil, for various values of the Reynolds number Re, aspect ratio A_R, wind tunnel upstream turbulence intensity Tu, wing setting inside the tunnel and maximum geometric blockage.
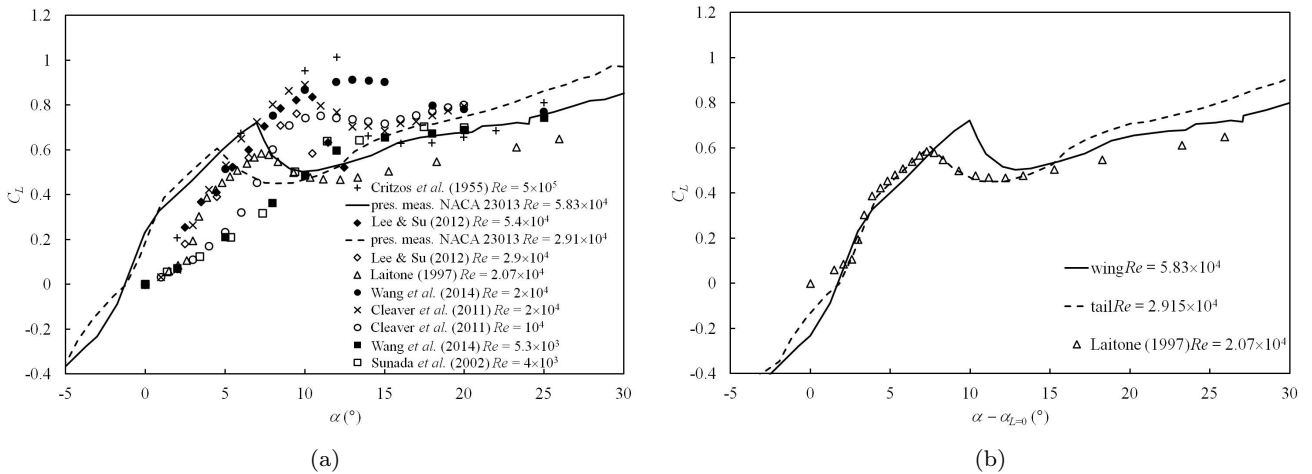

Fig. 7: Lift coefficient versus angle of attack, for the single wing and single tail NACA 23 012 airfoil and previous measurements on a NACA 0012 airfoil : (a) comparison of present measurements with previous investigations (Critzos et al (1955), Lee and Su (2012), Laitone (1997), Wang et al (2014), Cleaver et al (2011) and Sunada et al (2002)), (b) lift coefficient versus the angle of attack corrected by the zero lift angle of attack $\alpha - \alpha_{L=0}$, for similar wings, Reynolds number, wing setting and wind tunnel turbulence intensity (Laitone (1997)).

For α around 30°, a lower tail lift coefficient is observed in comparison with the single-tail configuration. These effects are typical of the two-airfoil arrangement and will be discussed in term of wake interaction and vortex shedding in section 6. For negative values, in the attached flow region, the lift coefficient magnitude is slightly lower than the lift coefficient observed for the single-tail arrangement. That light drop may be due to a downwash of the flow produced by the wing, providing a lower angle of attack in comparison with the single-tail arrangement. Very little change is observed in the drag coefficient in comparison with the single-wing or single-tail confiugation.
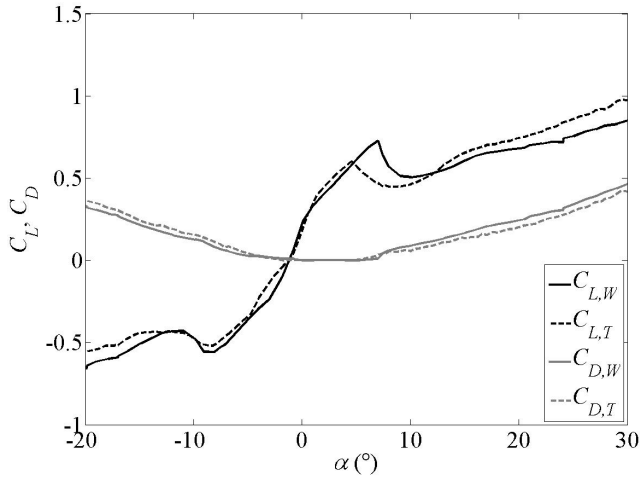
Fig. 8: Lift and drag coefficients for a single-wing or single-tail NACA 23 012 airfoil in the test section versus angle of attack.
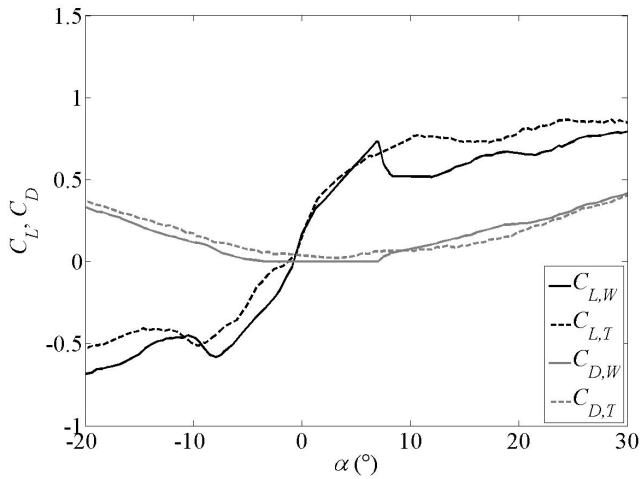

Fig. 9: Lift and drag coefficients for wing and tail NACA 23 012 airfoils in interaction in the test section versus angle of attack.

4.2 Interaction parameter

In order to quantify the aerodynamic interaction between the two airfoils, interaction parameters are defined for lift and drag coefficients as $(C_L - C_{L,S})/C_{L,S}$ and $(C_D - C_{D,S})/C_{D,S}$ with C_L and C_D the lift and drag coefficients for the two-airfoil arrangement and $C_{L,S}$ and $C_{D,S}$ the lift and drag coefficients for the single-airfoil arrangement. The development of the lift interaction parameter versus the angle of attack is given in figure 10. For values around the zero-lift angle of attack, the
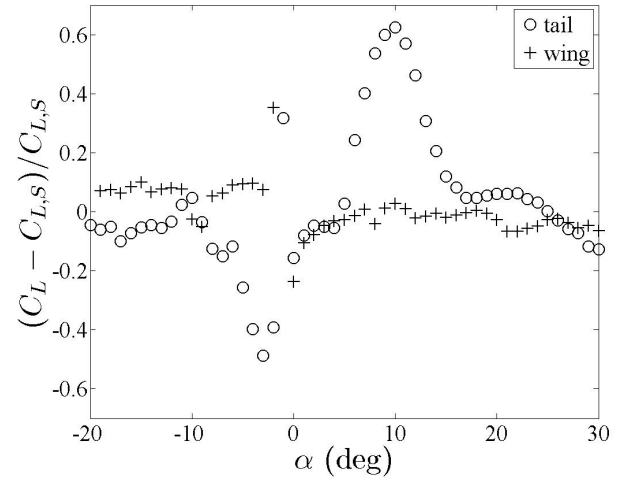

Fig. 10: Lift interaction parameter between the two-airfoil arrangement and the single-airfoil arrangement versus the angle of attack.

rise measured is simply due to very low values of the lift coefficient and the increase of the measurement noise. Except for these values of α, the interaction parameter of the wing is always between -0.1 and 0.1, which indicates the negligible forward potential effect caused by the tail on the wing. The behaviour is completely different for the tail, with a large increase of the interaction parameter from the stall angle of attack to $\alpha = 22°$. The maximum of the rise, with an increase larger than 0.6, is found for $\alpha = 10°$. Note a small negative value for α around $30°$. These feature are discussed hereafter in section 6. For negative values of the angle of attack, a decrease of the interaction parameter is observed with a minimum reached for $\alpha = -3°$, corresponding to the downwash produced by the wing.

The drag interaction parameter is presented in figure 11. For values of the angle of attack corresponding to an attached flow, the small values of drag result mainly in large values of the interaction parameter, which cannot be properly estimated. Except for that region, the drag interaction parameter is always between -0.1 and 0.1 for the wing, showing the negligible forward potential effect caused by the tail on the wing. For the tail, the values are bounded between -0.2 and 0.2, but a small drop of the drag coefficient is found between $\alpha = 10°$ and $20°$.

Few experimental studies about the interaction of a two-airfoil arrangement are available, they are summarised in table 2. For the present T-tail configuration, the stagger, obtained by the projection of the combination of L and H in the upstream flow direction for
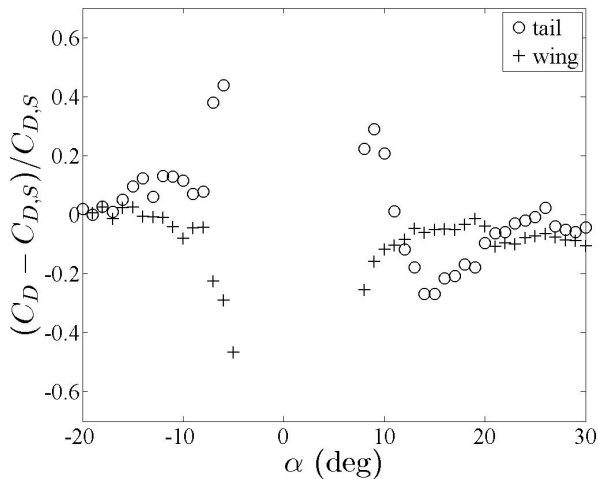
Fig. 11: Drag interaction parameter between the two-airfoil arrangement and the single-(in Khan and Mueller (1991) the downstream wing is between end plates and in Scharpf and Mueller (1992) both wings are between end plates)airfoil arrangement versus the angle of attack.

the different values of the angle of attack, is between 2.48 and 3.16, which is much more than the maximum value of 1.5 observed in previous investigations. Thus, a direct comparison of the aerodynamic coefficients or interaction parameters does not seems relevant, since the stagger and gap between the airfoils, are not in the same range.

The effect of the interaction between the two airfoils results in a rise of the lift for values around the tail stall angle. That point is to connect with the nature of the flow surrounding the tail, if it is placed behind the detached wing flow. A first possible explanation is that the tail is partially inside the wing wake with its pressure side in a lower velocity region, providing lower lift (note that the reference velocity for lift coefficients is always the velocity upstream from the wing). As for the wing, the flow is completely detached and the wake features a vortex shedding, another possible explanation of the lift rise of the tail may be given by the Kutta-Joukowski theorem, providing a direct link between lift and circulation. Then, the rise of the lift coefficient may be caused by the flow forcing, in the tail suction side, from the vortices generated upstream by the wing detached flow. As a consequence, the global circulation and lift coefficient are increased. In order to decide between these two options, additional analyses on the vortex shedding are necessary.

5 Vortex shedding

5.1 Vortex identification criterion

In order to understand the vortex shedding from wing and tail for detached flows values of the angle of attack, phase-averages are determined from the velocity fields. Phase-averaging is carried out with the identification of a vortex position. That analysis can be performed with time-resolved velocity fields (Faure et al (2010), Basley et al (2010)) or with not time-resolved fields synchronised with a one-point time-resolved signal, using a singular value decomposition (Faure et al (2006), Pastur et al (2008)). In the present study, an alternative method, not requiring synchronised measurements with a time-resolved signal, is adopted (Bourgoyne et al (2005)). A reference position along the normalised axial position x/c is chosen, corresponding to the full development of a detached vortex, together with an averaging spatial distance $\delta x/c$. All the vortices whose centres are located in the interval $[(x - \delta x)/c, (x + \delta x)/c]$ are considered inside the same class and their corresponding fields are averaged. Vortices are characterised on PIV fields with the Γ_2 criterion, which is a normalised kinetic moment defined by Graftieaux et al (2001) as:

$$\Gamma_2(\mathbf{x}) = \frac{1}{A} \int_{\xi \in A} \frac{(\xi - \mathbf{x}) \times [\mathbf{U}(\xi) - \mathbf{U}(\mathbf{x})]}{\|\xi - \mathbf{x}\| \times \|\mathbf{U}(\xi) - \mathbf{U}(\mathbf{x})\|} d\xi \qquad (2)$$

with $\mathbf{x}$ the position in the PIV field $\mathbf{U}$, A the integration area around that point and ξ the dummy integration variable. For PIV fileds, A is a PIV interrogation window (Faure (2014)). The denominator in that relation is very small if the streamlines have a small curvature radius, thus Γ_2 is noise sensitive in irrotational flow regions. In order to suppress that noise, Γ_2 is modified to zero in regions with vorticity below $0.4\ s^{-1}$. In the present experiment, the noise level is lower in comparison with previous literature (Panah and Buchholz (2014)) who considered a threshold of $4\ s^{-1}$. Then, Γ_2 values are smoothed inside a circle with a radius corresponding to two PIV interrogation windows. A search of a closed contour C is done in order to define the inner core of a vortex (Graftieaux et al (2001)), where the curve C is taken as the Γ_2 region where:

$$\frac{2}{\pi} \leq |\Gamma_2| \leq 1 \qquad (3)$$

The centre of a vortex is the barycentre of this closed contour. Then, Γ_2 fields development are decomposed into successive phases ϕ permitting to derived a phase time t in relation with the vortex shedding period T. With this identification criterion and the residual measurement noise, no noticeable vortex shedding is identified for values of the angle of attack lower than 15˚.

Researchers	Airfoil	c_W/c_T	Re	A_R	Tu (%)	Stagger	Gap
Khan and Mueller (1991)	FX63 − 137	0.66	1.5×10^5	2.8, 2.66	0.08	3	-0.5 to 0.5
Jones et al (2015)	flat plate	1	10^5	4	0.1	0 to 1.5	-1.5 to 1.5
Scharpf and Mueller (1992)	FX63 − 137	1	8.5×10^4	2.67	0.08	1.5	0
Lee (2011)	NACA 0012	1	8.5×10^4	2.53	not given	0.3	0
present meas.	NACA 23 012	2	5.83×10^4	9, 18	0.3	2.48 to 3.16	-0.87 to -0.83

Table 2: Experimental studies providing the lift coefficient for a two-airfoil arrangement, for various values of the chord ratio between the front and back airfoil c_W/c_T, Reynolds number Re, aspect ratio A_R, wind tunnel upstream turbulence intensity Tu and stagger and gap between the two airfoils (in Khan and Mueller (1991) the downstream wing is between end plates and in Scharpf and Mueller (1992) both wings are between end plates).

5.2 Phase averaging

That kind of decomposition is valid with only one reference period, associated with the vortex shedding frequency of the wing. For an angle of attack equal to 15°, the time-development of leading edge vortex (LEV) and trailing edge vortex (TEV) shedding from the wing is built in figure 12 for phase times $t/T = 0, 0.2, 0.4, 0.6, 0.8, 1$. For $t/T = 0.8$ near $x/c = 2$, a LEV is ejected from the shear layer above the suction side of the wing (figure 12d). That vortex is the result of the development of a Kármán instability. Then, it is advected downstream while a TEV is shed at $t/T = 0.2$ (figure12b). Note that the periodicity between LEV and TEV development is $t/T = 0.5$. These vortices shedding alternatively from the leading and trailing edges are mainly in interaction with the tail airfoil pressure side.

For an angle of attack $\alpha = 30°$, the Γ_2 criterion fields are given for the same phase times (figure 13). The tail airfoil is not completely immersed in the wing wake, and we note that the interaction results in a drop of the lift coefficient of the tail. For phase $t/T = 0$, the wing LEV is growing in the shear layer formed between the suction side recirculation and a TEV is developed but remains connected with the trailing edge (figure 13a). This TEV is ejected at $t/T = 0.2$ (figure 13b) and then advected in the flow. The wing LEV is ejected with a semi-period shift (figure 13e).

The positions of all the LEV and TEV centres created during the measuring time are plotted in figure 14 for the values of the angle of attack $\alpha = 15°$ and 30°. Note that there is no distinction between the centres emitted from the wing and the tail, as the vortex centres are obtained from the Γ_2 criterion on all the recorded fields. For $\alpha = 15°$ (figure 14a), the wing LEV and TEV are passing near the tail pressure side, their pathlines are converging on a point located below the tail, near

the trailing edge. Note the PIV shaddow region behind the tail where no centre is identified. Downstream of the tail, the centres observed are the LEV and TEV originating from the tail, whereas some of the LEV from the wing can be recognised as they are in line with the wing TEV. The similar result is presented for $\alpha = 30°$ in figure 14b, where the positions of the vortices emitted from the wing and from the tail are well separated. Similarly to $\alpha = 15°$, the pathlines of the wing LEV and TEV are not parallel, but are converging on a point placed above the tail.

5.3 Wing shedding vortex frequency

The shedding period T is measured from phased-averaged Γ_2 fields for the single-wing arrangement, considering a Taylor hypothesis assuming the advection of vortices by the upstream flow velocity:

$$T = \frac{d}{U_\infty} \tag{4}$$

with T the shedding period, U_∞ the upstream flow velocity and d the spacing between two successive detached LEV on the phase-averaged fields (figures 12 and 13). The corresponding Strouhal number is built as:

$$St = \frac{fc}{U_\infty} = \frac{c}{TU_\infty} \tag{5}$$

with f the shedding frequency. A second Strouhal number, based on the chord normal to the flow, is defined as:

$$St_\alpha = \frac{fc \sin \alpha}{U_\infty} \tag{6}$$

The development of Strouhal number versus the angle of attack is plotted in figure 15a and compared with measurements on NACA 0012 (Alam et al (2010)) and
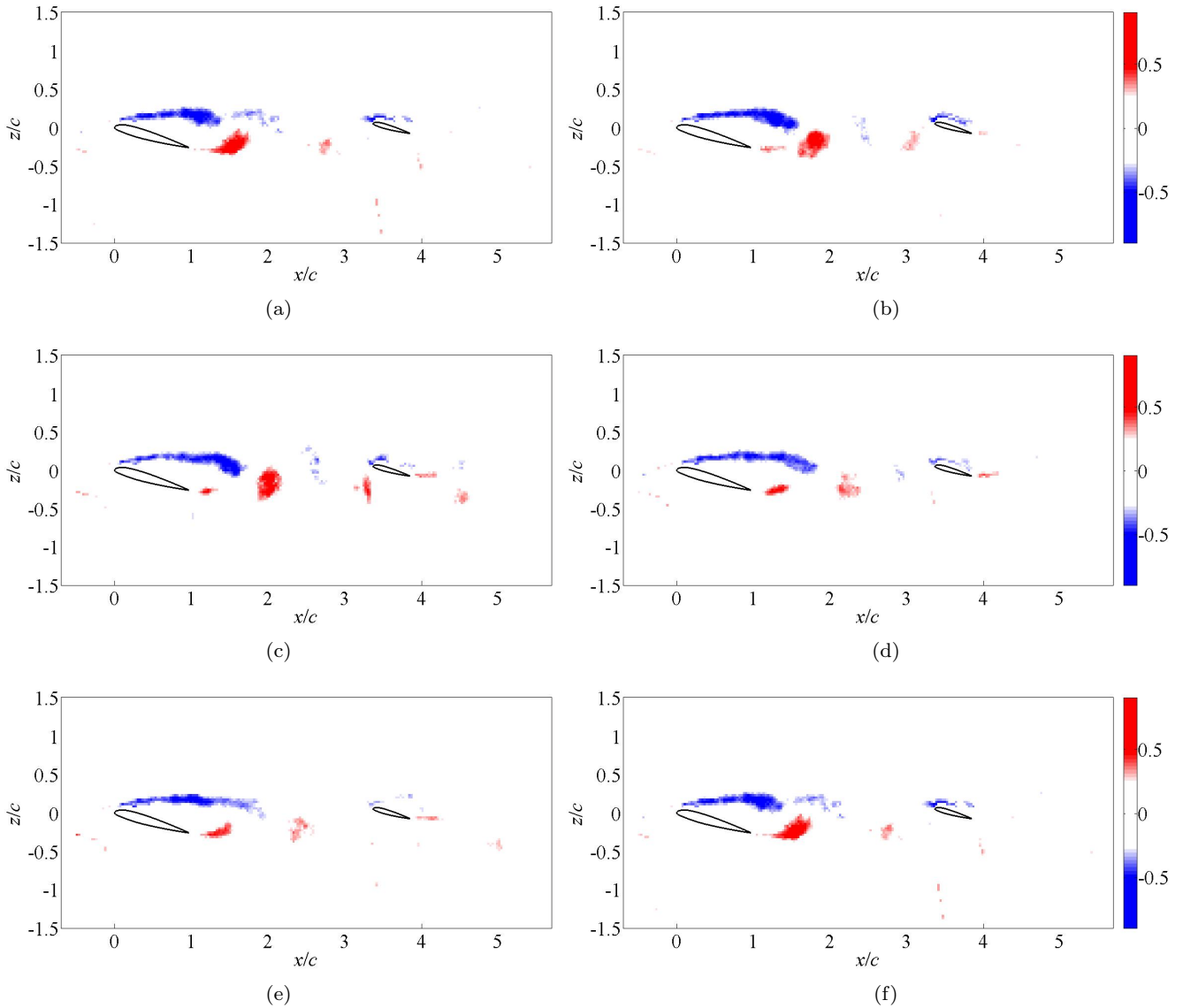
Fig. 12: Phase-averaged fields of the Γ_2 criterion for $\alpha = 15°$, $L = 3c$ and $H = c$ corresponding to (a) $t/T = 0$, (b) $t/T = 0.2$, (c) $t/T = 0.4$, (d) $t/T = 0.6$, (e) $t/T = 0.8$, (f) $t/T = 1$.

NACA $65_4 - 421$ airfoils (Sicot et al (2006)). A good arrangement of the measurement points is found, with a linear decrease of Strouhal number between $\alpha = 15°$ and $60°$ and a constant value of 0.12 for $\alpha > 60°$. The Strouhal number approaches that near constant value between 0.11 and 0.19 for the whole range of angle of attack if the Strouhal number based on the chord normal to the flow is used (figure 15b). Note that a Strouhal number between 0.17 and 0.21 is found downstream of a circular cylinder for a Reynolds number of 7.2×10^4 (Sumner et al (2008)).

5.4 Wing shedding vortex circulation

In order to quantify the vortex shedding, for the angles of attack corresponding to a detached flow on the wing, and its possible effect on the downstream tail, measurements of the LEV and TEV circulations are presented in this section. These values could be useful to validate potential methods based on discrete vortices (Sarpkaya (1975), Coronado Domenge and Ilie (2012), Ramesh et al (2014)). Few data are available in the literature for the circulation of shedding vortices downstream of a wing dominated by a detached flow, this information is generally presented for periodic wing motions. The cir-
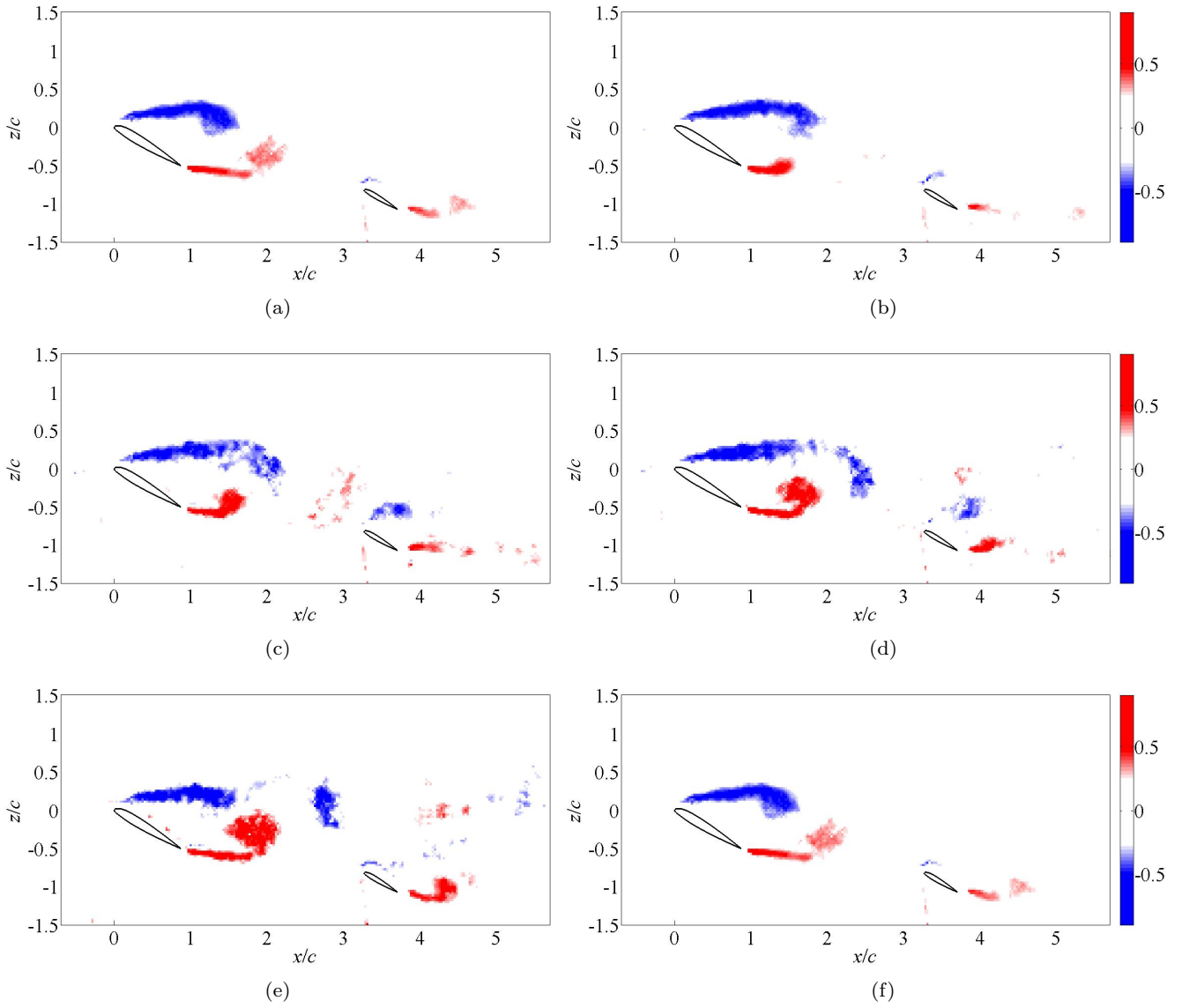
Fig. 13: Phase-averaged fields of the Γ_2 criterion for $\alpha = 30°$, $L = 3c$ and $H = c$ corresponding to (a) $t/T = 0$, (b) $t/T = 0.2$, (c) $t/T = 0.4$, (d) $t/T = 0.6$, (e) $t/T = 0.8$, (f) $t/T = 1$.
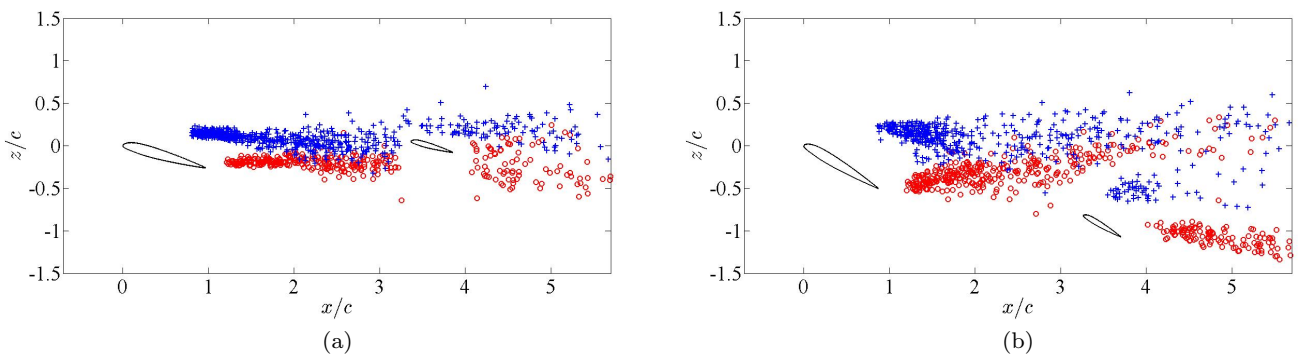

Fig. 14: Positions of the LEV ($+$) and TEV ($\bigcirc$) centres for $L = 3c$ and $H = c$: (a) $\alpha = 15°$, (b) $\alpha = 30°$.
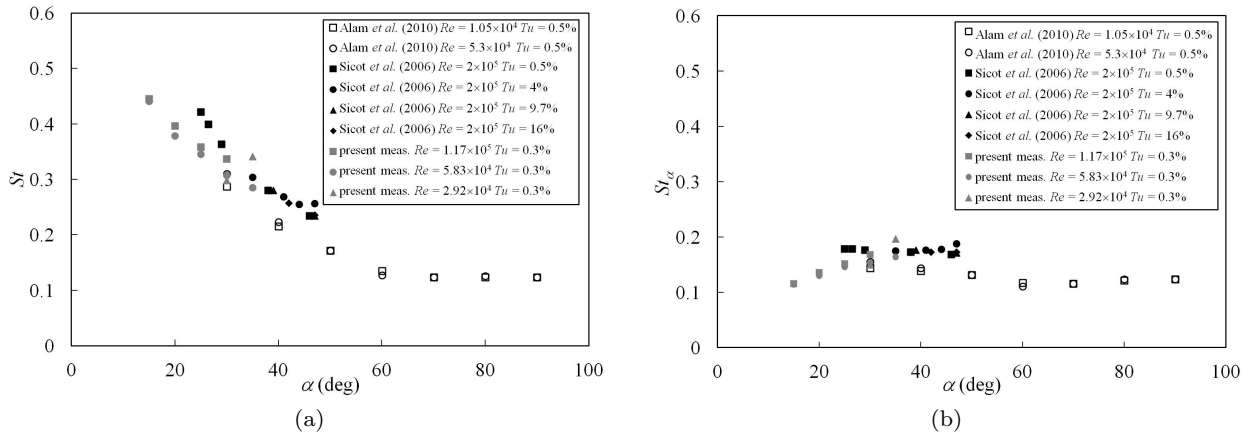
(a) (b)

Fig. 15: Vortex shedding Strouhal number versus angle of attack for NACA 0012 (Alam et al (2010)), NACA $65_4 - 421$ (Sicot et al (2006)) and NACA 23012 airfoils (present measurements): (a) Strouhal number, (b) Strouhal number based on the chord normal to the flow.

culation of the leading-edge and trailing-edge vortices along a bat's span for a Reynolds number $Re = 5 \times 10^3$ is presented in Muijres et al (2008) and downstream of a plunging SD 7003 airfoil for a Reynolds number $Re = 3 \times 10^4$ in Prangemeier et al (2010). In these studies, the flow unsteadiness is obtained by the flapping motion. A similar analysis of the circulation can be drown in the case of a detached flow on a constant angle of attack airfoil, where the unsteadiness results from the periodic vortex shedding.

The ciculation is defined as :

$$\Gamma = - \oint_C \mathbf{V}.\mathbf{d}\ell = - \iint_\Sigma \nabla \times \mathbf{V}.\mathbf{n} \, dS \qquad (7)$$

with $\mathbf{V}$ the velocity field and C the closed curve defined as Γ_2 levels greater than $2/\pi$ (section 5.1), Σ a surface which boundary is C and $\mathbf{n}$ a unit vector normal to Σ oriented according the right-hand rule for movment around C. The circulation of the LEV and TEV shedding from the wing, in the single-wing arrangement, are measured from the phase-averaged velocity fields (figure 16). Note that the phase reference is not necessary the same for each value of the angle of attack, since the position of the first vortex identified varies. Similarly to the case of a Von Kármán vortex street behind a circular cylinder (Von Kármán (1911)), the circulations between the upper and lower sides have the same order of magnitude and are opposite in sign. Note that the dispersion between the points may be caused by the integration of velocity along the contour C, but the difference between the LEV and TEV circulation, is lower than what was observed for flapping wings (Muijres et al (2008), Prangemeier et al (2010)), by a factor 4 for the LEV and a factor 8 for the TEV. That may be
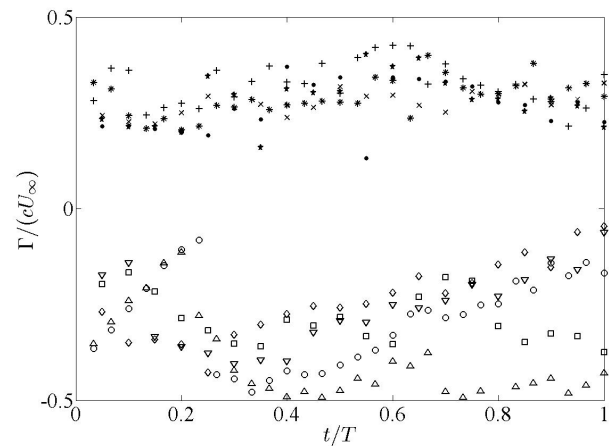

Fig. 16: LEV and TEV dimensionless circulation $\Gamma / (cU_\infty)$ versus the phase t/T for: $\alpha = 15°$,$\times$ LEV, $\square$ TEV; $\alpha = 20°$, + LEV, $\bigcirc$ TEV; $\alpha = 25°$, $*$ LEV, $\triangle$ TEV; $\alpha = 30°$, $\bullet$ LEV, $\triangledown$ TEV and $\alpha = 35°$, $\star$ LEV, $\diamond$ TEV.

caused by the different nature between the flapping motion of an attached flow on an airfoil, compared with present measurements concerning a constant angle of attack detached flow. For each value of the angle of attack, the LEV and TEV averaged circulation is obtained and its development with the angle of attack is given for two values of the Reynolds number in figure 17. Except for the TEV at $\alpha = 30°$ and $Re = 1.17 \times 10^5$, a point with large measurement noise, there is not a significant influence of the angle of attack on the circulation intensity. However, the Reynolds number seems to change the averaged value of the circulation.
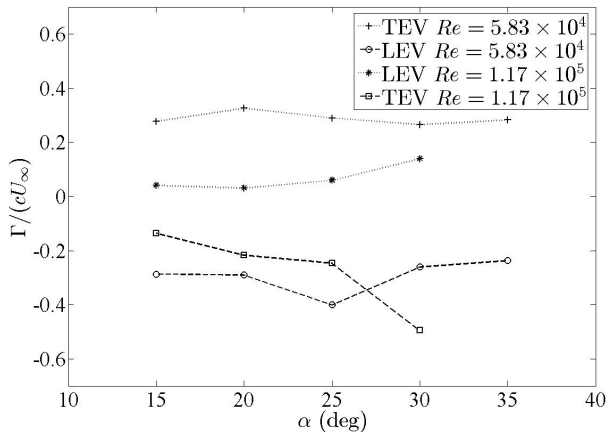
Fig. 17: Averaged leading edge and trailing edge vortex circulation of the upstream airfoil versus the angle of attack.

6 Flow forcing on the tail

The understanding of the increase of the tail lift coefficient in the range $5° \leq \alpha \leq 17°$ (figure 10), in the two-airfoil arrangement, is discussed in this section, in connection with the measured velocity fields (figure 5). For $\alpha = 5°$, the tail lift coefficient is increased in comparison with the single-tail arrangement, marked by the drop following the stall angle. The vortex shedding of LEV and TEV from the wing is not observed, if present it must be of small amplitude, with pathlines far from the tail, having little influence on its flow. The tail suction side could be partially detached, with an upstream flow velocity unchanged from the single-tail arrangement, while the tail pressure side could be influenced by the wing wake, corresponding to a lower velocity region. Then, the velocity on the pressure side V_{ps} could decrease and the tail lift coefficient increase from the single-tail arrangement (figure 18a). A similar analysis could be made for $\alpha = 10°$, where the maximum increase in tail lift coefficient is found (figure 10). The suction side of the tail is completely detached with an upstream flow velocity unchanged from the single-tail arrangement, while the tail pressure side could be influenced by the wing wake, corresponding to a lower velocity region. The velocity on the pressure side could be decreased and the tail lift coefficient increased from the single-tail arrangement (figure 18b). The explanation of the lift increase could be different for $\alpha = 15°$. In that arrangement, the wing is completely detached and a shedding of LEV and TEV established (figure 14a). In addition, the tail is completely immersed inside the wing wake, and its suction side could be periodically reattached by the wing LEV shedding, that reattache-

ment inducing an increase of the tail lift coefficient. On the tail pressure side, the flow is attached, but a periodic shedding of the wing TEV could induce a decrease of velocity and an increase of pressure resulting in a global increase in the tail circulation and lift coefficient (figure 18c). For $\alpha = 30°$, the wing TEV and LEV shedding are relatively far from the tail (figure 14b) and may have little influence on its lift coefficient. However, the detached tail suction side is close to the wing wake and lower velocities could be found in comparison with the single-tail arrangement. That effect could explain a sligtly lower suction side velocity V_{ss}, resulting in a sligtly lower circulation and lift coefficient (figure 18d).

7 Conclusion

A reference 2D experiment, developed to understand the interaction between a wing and a tail for a T-tail aircraft configuration, is implemented in a wind tunnel. Measurements include PIV velocity fields, which are not time-resolved, and lift and drag forces on each airfoil.

A statistical analysis of the velocity fields presents the development of the recirculation region with the angle of attack, with a strong increase in velocity defect, wake width and turbulence level for detached flow configurations. For the present stagger and gap arrangement, the tail is placed inside the wing wake for $\alpha = 15°$. Around this value, the classical lift coefficient drop observed on the tail after the stall angle disappears, resulting from the interaction with the upstream wing. For $\alpha = 30°$, a slight decrease of the lift coefficient for the two-airfoil arrangement is observed.

Two possible effects are identified on the tail: a wake influence or a vortex forcing. Phase-averages of the Γ_2 fields show the periodic vortex shedding corresponding to the development of a Kármán instability for angles of attack larger than 15°. A Strouhal number is build from the phase averaged fields, providing a good agreement with previous experiments to give measurements in the range $0.11 \leq St_\alpha \leq 0.19$. The LEV and TEV circulations are also obtained from the velocity fields. The time-averaged circulation of the vortices does not seem to change with the angle of attack, as long as the flow is detached on the wing, but its magnitude seems to increase with Reynolds number.

The analysis of velocity fields and shedding vortex dynamics lead to the understanding of changes in the tail lift coefficient development with angle of attack, for the two-airfoil arrangement, in comparison with the single-tail setting, and can be summarised as follows. For α between 4° and 10°, no noticeable vortex shedding is observed and the increase of the tail lift coefficient is mainly due to the influence of the wing wake, on
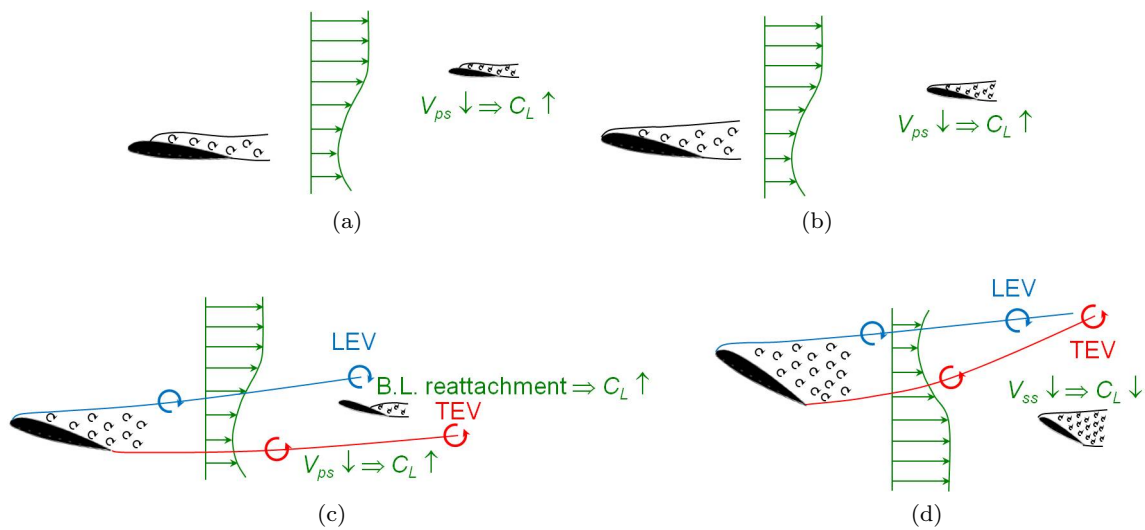
Fig. 18: Sketches of the flow development around the tail for $L = 3c$ and $H = c$ corresponding to (a) $\alpha = 5°$, (b) $\alpha = 10°$, (c) $\alpha = 15°$, (d) $\alpha = 30°$.

the tail pressure side. For $\alpha = 15°$, the wing LEV pathlines are near the tail suction side, leading to a vortex forcing and a positive lift variation in comparison with the single-tail arrangement. For $\alpha = 30°$, the wing TEV and LEV shedding are relatively far from the tail and may have little influence on its lift coefficient, but the tail suction side is inside the border of the wing wake, resulting in a lower circulation in comparison with the single-tail case.

References

Abbott IHA, Von Doenhoff AE (1949) Theory of Wing Sections, Including a Summary of Airfoil Data. Dover Publications

Alam MM, Sakamoto H (2005) Investigation of Strouhal frequencies of two staggered bluff bodies and detection of multistable flow by wavelets. Journal of Fluids and Structures 20(3):425–449

Alam MM, Zhou Y, Yang HX, Guo H, Mi J (2010) The ultra-low Reynolds number airfoil wake. Experiments in Fluids 48(1):81–103

Anderson JM, Streitlien K, Barrett DS, Triantafyllou MS (1998) Oscillating foils of high propulsive efficiency. Journal of Fluid Mechanics 360:41–72

Basley J, Pastur LR, Lusseyran F, Faure TM, Delprat N (2010) Experimental investigation of global modes in an incompressible cavity flow using time-resolved PIV. Experiments in Fluids 50(4):905–918

Bourgoyne DA, Hamel JM, Ceccio SL, Dowling DR (2003) Time-averaged flow over a hydrofoil at

high Reynolds number. Journal of Fluid Mechanics 496:365–404

Bourgoyne DA, Ceccio SL, Dowling DR (2005) Vortex shedding from a hydrofoil at high Reynolds number. Journal of Fluid Mechanics 531:293–324

Cleaver DJ, Wang Z, Gursul I, Visbal M (2011) Lift enhancement by means of small-amplitude airfoil oscillations at low Reynolds numbers. AIAA Journal 49(9):2018–2033

Coronado Domenge PX, Ilie M (2012) Numerical study of helicopter blade-vortex mechanism of interaction using the potential flow theory. Applied Mathematical Modelling 36:2841–2857

Critzos CC, Heyson HH, Boswinkle Jr RW (1955) Aerodynamic characteristics of NACA 0012 airfoil section at angles of attack from 0 degrees to 180 degrees. Tech. rep., NACA TN 3361

Devinant P, Laverne T, Hureau J (2002) Experimental study of wind-turbine airfoil aerodynamics in high turbulence. Journal of Wind Engineering and Industrial Aerodynamics 90(6):689–707

Faure TM (2014) Velocity field and parametric analysis of a subsonic, medium-Reynolds number cavity flow. Experiments in Fluids 55(11):1822

Faure TM, Lusseyran F, Pastur L, Debesse P (2006) Développement d'instabilités dans un écoulement subsonique se développant au-dessus d'une cavité : mesures synchronisées PIV-LDV. In: 10e Congrès Francophone de Techniques Laser, Toulouse, France

Faure TM, Thach H, Basley J, Pastur L, Lusseyran F (2010) Moyenne de phase spatiale appliquée à des champs PIV résolus en temps. In: 12e Congrès Fran-

cophone de Techniques Laser, Nancy, France, pp 111–118

Favier D, Maresca C, Barbi C, Castex A (1987) Vortex influence on oscillating airfoils at high angle of attack. Journal of Aircraft 24(7):424–432

Graftieaux L, Michard M, Grosjean N (2001) Combining PIV, POD and vortex identification algorithms for the study of unsteady turbulent swirling flows. Measurement Science and Technology 12(9):1422

Hétru L (2015) Étude expérimentale et numérique de l'interaction aérodynamique entre deux profils : application au risque aéronautique du décrochage profond. PhD thesis, Université d'Aix-Marseille

Horner MB, Saliveros E, Galbraith R (1993) An examination of vortex convection effects during blade-vortex interaction. Zeitschrift fur Flugwissenschaften und Weltraumforschung 17(3):189–195

Hu J, Zhou Y (2008a) Flow structure behind two staggered circular cylinders. part 1. downstream evolution and classification. Journal of Fluid Mechanics 607:51–80

Hu J, Zhou Y (2008b) Flow structure behind two staggered circular cylinders. part 2. heat and momentum transport. Journal of Fluid Mechanics 607:81–107

Huang RF, Lee HW (2000) Turbulence effect on frequency characteristics of unsteady motions in wake of wing. AIAA Journal 38(1):87–94

Huang RF, Lin CL (1995) Vortex shedding and shear-layer instability of wing at low-Reynolds numbers. AIAA Journal 33(8):1398–1403

Jones R, Cleaver D, Gursul I (2015) Aerodynamics of biplane and tandem wings at low Reynolds numbers. Experiments in Fluids 56(124)

Katz J, Plotkin A (2001) Low-Speed Aerodynamics. Cambridge University Press

Khan F, Mueller T (1991) Tip vortex/airfoil interaction for a low Reynolds number canard/wing configuration. Journal of Aircraft 28(3):181–186

Laitone EV (1997) Wind tunnel tests of wings at Reynolds numbers below 70 000. Experiments in Fluids 23(5):405–409

Lee T (2011) Flow past two in-tandem airfoils undergoing sinusoidal oscillations. Experiments in Fluids 51(6):1605–1621

Lee T, Su Y (2012) Low Reynolds number airfoil aerodynamic loads determination via line integral of velocity obtained with particle image velocimetry. Experiments in Fluids 53(5):1177–1190

Mueller TJ, DeLaurier JD (2003) Aerodynamics of small vehicles. Annual Review of Fluid Mechanics 35(1):89–111

Muijres FT, Johansson LC, Barfield R, Wolf M, Spedding GR, Hedenström A (2008) Leading-edge vortex improves lift in slow-flying bats. Science 319(5867):1250–1253

Panah AE, Buchholz JHJ (2014) Parameter dependence of vortex interactions on a two-dimensional plunging plate. Experiments in Fluids 55(3):1–19

Pastur L, Lusseyran F, Faure TM, Fraigneau Y, Pethieu R, Debesse P (2008) Quantifying the nonlinear mode competition in the flow over an open cavity at medium Reynolds number. Experiments in Fluids 44(4):597–608

Prangemeier T, Rival D, Tropea C (2010) The manipulation of trailing-edge vortices for an airfoil in plunging motion. Journal of Fluids and Structures 26(2):193–204

Ramesh K, Gopalarathnam A, Granlund K, Ol MV, Edwards JR (2014) Discrete-vortex method with novel shedding criterion for unsteady aerofoil flows with intermittent leading-edge vortex shedding. Journal of Fluid Mechanics 751:500–538

Ravi S, Watkins S, Watmuff J, Massey K, Petersen P, Marino M, Ravi A (2012) The flow over a thin airfoil subjected to elevated levels of freestream turbulence at low Reynolds numbers. Experiments in Fluids 53(3):637–653

Sarpkaya T (1975) An inviscid model of two-dimensional vortex shedding for transient and asymptotically steady separated flow over an inclined plate. Journal of Fluid Mechanics 68(1):109–128

Scharpf DF, Mueller TJ (1992) Experimental study of a low Reynolds number tandem airfoil configuration. Journal of Aircraft 29(2):231–236

Sicot C, Aubrun S, Loyer S, Devinant P (2006) Unsteady characteristics of the static stall of an airfoil subjected to freestream turbulence level up to 16%. Experiments in Fluids 41(4):641–648

Sumner D (2010) Two circular cylinders in cross-flow: a review. Journal of Fluids and Structures 26(6):849–899

Sumner D, Price S, Paidoussis M (2000) Flow-pattern identification for two staggered circular cylinders in cross-flow. Journal of Fluid Mechanics 411:263–303

Sumner D, Richards M, Akosile O (2008) Strouhal number data for two staggered circular cylinders. Journal of Wind Engineering and Industrial Aerodynamics 96(6):859–871

Sunada S, Yasuda T, Yasuda K, Kawachi K (2002) Comparison of wing characteristics at an ultralow Reynolds number. Journal of Aircraft 39(2):331–338

Świrydczuk J (1990) A visualization study of the interaction of a free vortex with the wake behind an airfoil. Experiments in Fluids 9(4):181–190

Taylor RT, Ray EJ (1965) Deep-stall aerodynamic characteristics of T-tail aircraft. NASA Conference on

Aircraft Operating Problems SP-83:113–121

Von Kármán T (1911) Über den Mechanismus des Widerstandes, den ein bewegter Körper in einer Flüssigkeit erfährt. Nachrichten von der Gesellschaft der Wissenschaften zu Göttingen, Mathematisch-Physikalische Klasse pp 509–517

Wang S, Zhou Y, Alam MM, Yang H (2014) Turbulent intensity and Reynolds number effects on an airfoil at low reynolds numbers. Physics of Fluids 26(11):115,107

West GS, Apelt CJ (1982) The effects of tunnel blockage and aspect ratio on the mean flow past a circular cylinder with Reynolds numbers between 10^4 and 10^5. Journal of Fluid Mechanics 114:361–377

Wu JZ, Lu XY, Denny AG, Fan M, Wu JM (1998) Post-stall flow control on an airfoil by local unsteady forcing. Journal of Fluid Mechanics 371:21–58

Yarusevych S, Sullivan PE, Kawall JG (2009) On vortex shedding from an airfoil in low-Reynolds-number flows. Journal of Fluid Mechanics 632:245–271

Zhou Y, Alam MM (2016) Wake of two interacting circular cylinders: A review. International Journal of Heat and Fluid Flow 62:510–537